Near-Infrared Luminescent Ru(II) and Os(II) Complexes

Salwa Simona Jamil, Valerio Giuso, Christophe Gourlaouen, Matteo Mauro, Cristina Cebrián, Philippe C. Gros

Near-Infrared Luminescent Ru(II) and Os(II) Complexes

Salwa Simona Jamil,[a] Valerio Giuso,[b] Christophe Gourlaouen,[c] Matteo Mauro,*[d,b] Cristina Cebrián,*[e] and Philippe C. Gros*[a]

[a] Dr. P.C. Gros, Dr. S. S. Jamil
Université de Lorraine, CNRS, L2CM, 54000 Nancy (France)
E-mail: philippe.gros@univ-lorraine.fr

[b] V. Giuso, Prof. Dr. M. Mauro
Université de Strasbourg, CNRS, IPCMS, 67034 Strasbourg (France)

[c] Dr. C. Gourlaouen
Université de Strasbourg, CNRS, CMC, 67081 Strasbourg (France)

[d] Prof. Dr. M. Mauro
University of Padova, Department of Chemical Sciences, 35121 Padova, (Italy)
E-mail: matteo.mauro@unipd.it

[e] Dr. C. Cebrián
Université de Strasbourg, CNRS, ICS, 67034 Strasbourg (France)
E-mail: ccebrianavila@unistra.fr

Supporting information for this article is given via a link at the end of the document.

Abstract: Two Ru(II) and Os(II) homoleptic complexes based on a phenanthroline-pyridylidene tridentate ligand have been designed to reach NIR emission by combining strong σ-donation, provided by the unconventional *N*-heterocyclic carbene (NHC) pyridylidene moiety, with the low-lying π-accepting phenanthroline scaffold. Detailed experimental and computational investigations of the photophysical properties of this novel family of cyclometallated complexes reveal emission squarely falling in the NIR domain peaking at λ_{em} = 790 nm for the Os(II) complex, while emission is hypsochromically shifted at λ_{em} = 747 nm for the Ru(II) homologue in deareated CH_3CN solution at room temperature. Despite the triplet metal-to-ligand charge transfer (^{3}MLCT) nature that characterizes the excited state in both complexes, density functional theory (DFT) calculations allow to ascribe the remarkable optical shift observed in the latter to the larger spin-orbital coupling (SOC) effects exerted by the heavier metal.

Introduction

The development of photoactive transition metal complexes is a continuously growing area driven by their application is various fields, such as solar energy conversion,[1–3] photocatalysis,[4–6] photoelectrochemistry,[3,7] bioimaging[8,9] and light-emitting devices (*e.g.* organic light emitting diodes and light emitting electrochemical cells).[10–12] In the field of luminescent complexes, great achievements have been obtained to date in the green to red region of the visible spectrum in terms of both photoluminescence quantum yield (PLQY), (photo)stability and redox modulation. Nevertheless, designing compounds that display efficient deep-red or even to near infrared (NIR) luminescence is significantly more challenging and examples are still limited.[13–15] On the one hand, the value of the associated radiative rate constant, k_r, that characterizes the emissive excited state is intrinsically small since it scales with the third-power of the energy of the emitted photon, as by Einstein's theory of spontaneous emission.[16] On the other hand, the vibronic coupling between T_1 and ground, S_0, state is very efficient due to the negative Napierian logarithmic dependency with the T_1–S_0 energy difference (*energy gap law*), yielding large values of the non-radiative rate constant, k_{nr}.[17] Therefore, judicious molecular designs are required to overcome the typical very poor emission efficiencies associated to such low-energy emissions.[13,14]

To this aim, octahedral low-spin d^6 complexes of Ru(II) and Os(II) have been found of particular interest.[14,18–20] These species possess low-lying triplet metal-to-ligand charge transfer (^{3}MLCT) excited states with relatively long-lived excited-state lifetimes. When comparing archetypal polypyridyl complexes of general formula $[M(N^N)_3]^{2+}$, where N^N are diimine type of ligands, ruthenium complexes are more likely to exhibit thermally accessible triplet metal-centered (^{3}MC) excited states, efficiently acting as non-radiative channels as well as compromising thermal and photostability.[21] The barrier can nevertheless be raised upon introduction of electron-donating and -accepting substituents,[22] selection of strong-field ligands[23–25] or improvement of ligand-metal interaction by employing ligand scaffolds that would enable a closer-to-ideal octahedral geometry.[26–28] As for the osmium counterparts, the exerted ligand field (*ca.* 30% more intense than ruthenium) pushes ^{3}MC states to higher energies.[29] However, Os(II) derivatives often display poorer PLQY due to the fact that its lower reduction potential leads to lower-lying ^{3}MLCT, thus being more affected by the energy gap law.[30] Furthermore, these heavy metal ions present sizeable spin-orbit coupling (SOC) constant (ζ_{Ru} = 1100 cm^{-1}, ζ_{Os} = 3000 cm^{-1}) that favors formally spin-forbidden transitions, especially in the case of the latter metal.[21]

As far as NIR emissive Ru and Os complexes are concerned, several design strategies have been proposed to reduce the energy of the ^{3}MLCT states, formally originated from the electron density displacement from a d_π(M) into a π_L* antibonding orbital. Some selected examples are shown in Figure 1, with their key photophysical data being collected in Table S1. Extension of the π-conjugated system of the chromophoric ligands[31–33] and the introduction of electron-withdrawing groups and/or heteroatoms[34–36] have both proven useful approaches in stabilizing the ligand-centered π* orbitals. However, the intrinsic high-energy 5d orbitals in comparison to 4d orbitals renders attaining phosphorescence in the NIR region easier for Os(II) complexes than for the Ru(II) analogs. For instance, the homoleptic complex of 4,4'-diphenyl-2,2'-bipyridine **Os1** displays an emission at λ_{em} = 765 nm with a PLQY of 1.7%, while the emission of **Ru1** appears hypsochromically shifted by 2700 cm^{-1} (λ_{em} = 634 nm and PLQY = 29.3%).[37] Nevertheless, this strategy presents its limitations as nicely illustrated by the work of Elliott, Scattergood and co-workers,[38] which investigated the impact of the ligand π-deficiency on the emissive properties of Os(II) compounds. As shown by **Os2a** and **Os2b**, the increased accepting character in the latter favored a concomitant stabilization of the metal-based HOMO through π-backdonation, thereby resulting in an emission profile that is hypsochromically shifted by 442 cm^{-1}.

A second approach to achieve low-energy emission consists in the destabilization of the HOMO induced by (formally) anionic ligands, which is particularly useful in the case of Ru(II) complexes as previously stated.[24,33,36,39–41] Sauvage and co-workers described one of the first examples of cyclometallated Ru(II) complexes with NIR emission (**Ru2**), where the increased rigidity afforded by the interligand π– π interactions between the terpyridine and tolyl (Tol) moieties plays a non-negligible role in preserving room-temperature NIR luminescence.[23,42] The use of azolates as an alternative to cyclometallated rings has been thoroughly studied by Chi, Chou and co-workers for both metals as shown in **Ru3**[43] and **Os3**.[44] These units not only provide a strong σ-interaction as cyclometallating rings, but also present the advantage of an easier obtention respect to the latter due to the N–H acidity of the parent azole unit.[45] Interestingly, both compounds exhibit emissions approaching 800 nm with remarkable efficiencies in the solid state (λ_{em} = 795 and 779 nm, PLQY = 2% and 4.5% for **Ru3** and **Os3**, respectively).

Apart from the previous approaches, lowering the symmetry of either the ligands or the complexes yields often a further bathochromic shift of the emission.[36,38,46–49] As a matter of example, heteroleptic **Ru4** complex features a strong donor ligand together with an accepting terpyridine (tpy), achieving a remarkable NIR emission (λ_{em} = 900 nm), yet with PLQY as low as 0.1%.[35]

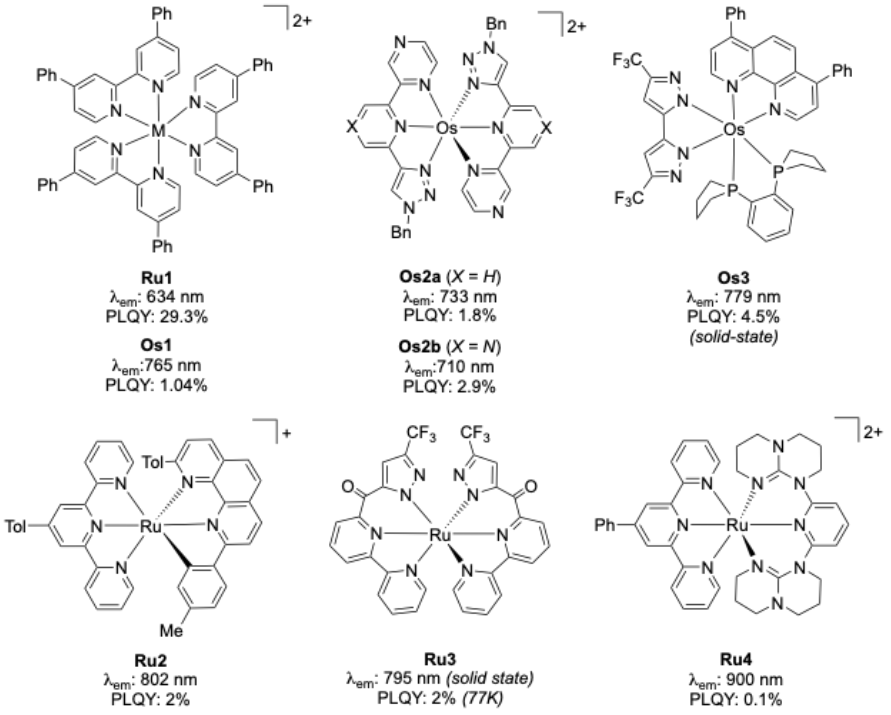

Figure 1. Selected examples of NIR emissive Ru(II) and Os(II) complexes along with their main photophysical data.

In the last decades, *N*-heterocyclic carbenes (NHC) have emerged as a leading class of ligands for designing efficient emitters due to their ability to engage into robust metal-ligand bonds along with their large synthetic versatility in terms of both electronic and steric features.[50–53] Moreover, their strong σ-donation features lead to higher d-d* orbitals splitting, thereby destabilizing the nonradiative MC excited states and enhancing the emissive properties of the corresponding complexes.[51] Ru(II) complexes bearing NHC ligands illustrate this effect well, often presenting significantly enhanced emission lifetimes compared to their polyimine analogues as a result of an increased ^{3}MLCT–^{3}MC energy gap.[25,54,55] However, the high energy π* orbitals of NHC units[56] may lead to an hypsochromic shift of the luminescence as described for some Ru(II)[54] and Os(II)[57] complexes, although this effect can be cancelled out by adopting a heteroleptic design.[58,59]

Among the wide palette of NHCs, the pyridylidene scaffold remains rather unexplored to date. This is despite its stronger σ-donor and π-acceptor character compared to that of the widely studied imidazolidinylidenes, imidazolylidenes and their (benz)annulated derivatives.[60] Thus, we herein report on the synthesis and comprehensive characterization of a novel tridentate C^N^N scaffold comprising a cyclometallating pyrid-2-ylidene (C) and a 1,10-phenanthroline (N^N) units. We anticipate that the strong σ-donation of the former helps for pushing up the quenching ^{3}MC states, while the π-accepting character of the latter pulls

down the π* orbitals. Aiming at novel d^6 organometallic complexes that feature emission into the NIR region, this NHC-based C^N^N chromophoric ligand was investigated for the formation of the corresponding homoleptic Ru(II) and Os(II) complexes of general formula $[M(C^N^N)_2](PF_6)_2$, namely **[Ru]** and **[Os]**, the latter being the first example of its kind to the best of our knowledge (Scheme 1). Their optical properties were investigated in detail by means of steady state and time resolved photophysical techniques, confirming the NIR emission and the suitable molecular design strategy compared to other NHC-based ligands. Finally, the electronic and optical properties were further elucidated in the frame of density functional theory (DFT) methods that highlighted the important role played by the spin-orbit coupling (SOC) perturbation in modulating the optical properties into the NIR.

Results and Discussion

Synthesis characterization

The general synthetic pathway employed for the preparation of the target ligand and complexes is depicted in Scheme 1 (see Supporting Information for further details). At a first stage, the synthesis required the preparation of the pyridinium proligand **HL** that was readily obtained in excellent yield by heating a neat mixture of 2-bromophenanthroline and 4-(*tert*-butyl)pyridine, followed by a metathesis reaction with a saturated solution of KPF_6. Subsequently, the complexation was achieved by direct metalation of **HL** with the corresponding metal trichloride in a 2:1 ratio in hot ethylene glycol for 16 hours. The complexes were obtained as their hexafluorophosphate salts and purified by column chromatography followed by crystallization using dichloromethane and diethylether. Complexes **[Ru]** and **[Os]** were obtained in reaction yield of 37% and 60%, respectively. In contrast to previous reports, addition of a strong Brønsted base was not necessary in this case confirming the milder condition required for the synthesis of the target complexes.[61,62]

Well-resolved ^1H and $^{13}C\{^1H\}$ NMR spectra of both complexes were obtained, strongly supporting diamagnetic low-spin d^6 nature of the complexes. The chemical shifts were fully assigned using ^1H-^1H COSY experiments (see Figure S5 and Figure S8 of the Supporting Information). ^1H NMR spectra recorded in acetonitrile-d_3 solution were characterized by one singlet signal at δ = 0.88 and 0.90 ppm for **[Ru]** and **[Os]**, respectively, corresponding to the *tert*-butyl group and the expected ten different resonances in the aromatic region. While the cyclometallation was clearly evidenced by the loss of the pyridine α-proton (H1), the carbene nature was reflected by the strong upfield shift of the pyridine β-proton (H2), due to a reduced π-delocalization,[63] peaking at δ = 6.27 and 6.16 ppm for **[Ru]** and **[Os],** respectively (see Scheme 1 for partial atom labeling). A remarkable difference was also noticed in the $^{13}C\{^1H\}$ NMR spectra of **[Ru]** and **[Os]** for the metalated carbon atom (M–C), where M = Ru, Os, that displays a resonance at δ = 211 and 188 ppm, respectively. In comparison to the chemical shift of a free pyridylidene,[64] the ligand in **[Ru]** shows a more pronounced carbene-like character.[65] The shift of Δδ = 23 ppm to higher fields when going from **[Ru]** to **[Os]** reflects a reduction of the anisotropy at the carbene atom, which can be attributed to the higher covalency of the Os–C bond.[66] The high-resolution electrospray mass spectrum (HR-ESI-MS) of **[Ru]** and **[Os]** showed the expected isotopic distribution of peaks (see Figure S9 and Figure S10 of the Supporting Information).[67]

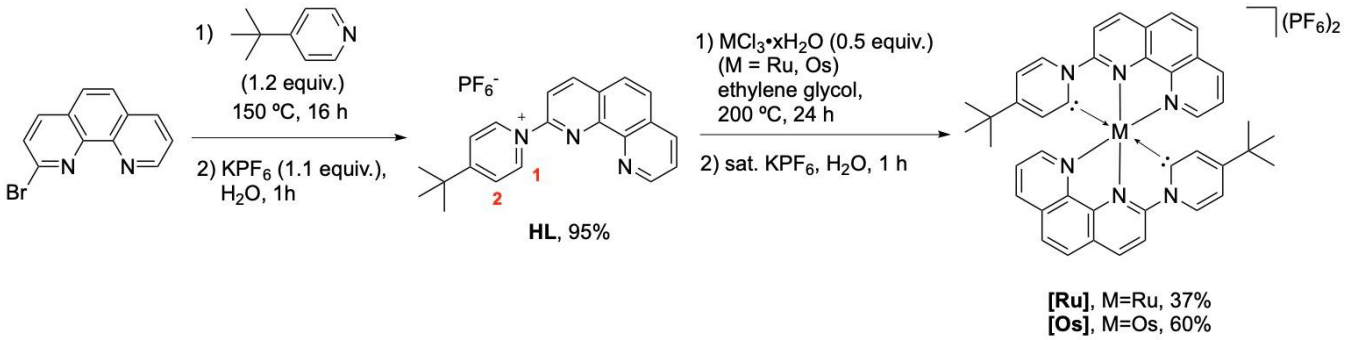

Scheme 1. Synthesis of the target ligand **HL** and the corresponding Ru(II) and Os(II) complexes **[Ru]** and **[Os]**.

Single crystals of suitable quality for X-ray diffractometric analysis were obtained by solvent/non-solvent vapour diffusion method using dichloromethane and diethylether. The crystal structures of complexes **[Ru]** and **[Os]** are depicted in Figure 2, and the bond distances and angles related to the coordination sphere are summarized in Table 1 (see Tables S2–S3 for full crystallographic details). The compounds crystallize as pairs of enantiomers in orthorhombic and triclinic space groups $Pna2_1$ and $P\bar{1}$ for **[Ru]** and **[Os]**, respectively, with an additional molecule of diethylether being present in the former. Stronger anion-π interactions can be identified within the crystal structure of **[Ru]**.[68] Interestingly, these non-covalent interactions involve a different heteroaromatic unit, *i.e.* the phenanthroline unit in **[Ru]** (Figure S11) and the pyrid-2-ylidene unit in **[Os]** (Figure S12), which might explain their different solid-state fluorescence behavior (*vide infra*).

As for the complex cation, the metal ion is found in a distorted octahedral geometry with the tridentate ligands coordinated in a meridional fashion, resulting in N(1)–M–C(21) bite angles of 155.1(3)–156.0(3)º that are far from the 180º of an ideal octahedron. The pyridylidene nature of the ligand is reflected by the reduced carbene N–C(21)–C(20) angle, with values *ca.* 114º.[63,69] Average M–C bonds are in accordance with those previously reported in other M–pyridylidene complexes [1.946–2.033 Å].[62,64,65,69–71] The M–N(1) bonds appear systematically elongated (*ca.* 0.1 Å) in comparison with the corresponding $[M(tpy)_2]^{2+}$ complexes[72,73] as a result of the trans influence imparted by the NHC unit. However, this effect is more important in **[Ru]** than in **[Os]**, being M–N(1) mean values *d* = 2.199 and 2.165 Å, respectively. This effect can be ascribed to the higher carbene-like character of the former. The less distorted geometry in the Os(II) compound is also evidenced by the almost perpendicular configuration of the ligands in **[Os]** with N(2A)–M–N(2B) = 168.8(3) and 176.4(3)º for **[Ru]** and **[Os]**, respectively. Nevertheless, this might be just a mere crystal packing effect.

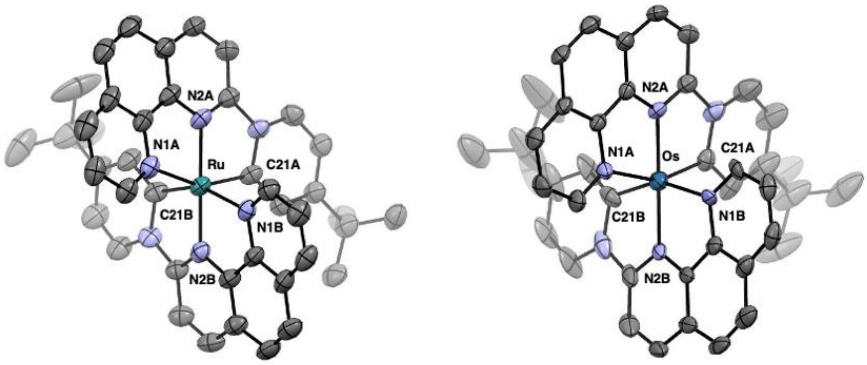

Figure 2. ORTEP representations of the X-ray crystal structures of **[Ru]** (left, CCDC: 2431775) and **[Os]** (right, CCDC: 2431780). Thermal ellipsoids are shown at 50% probability. Hydrogen atoms, solvent molecules and PF_6^- anions are omitted for clarity.

Table 1. Selected bond lengths [Å] and angles [°] for **[Ru]** and **[Os]**.

	[Ru]	**[Os]**
d(M–C21A)	1.983(9)	2.017(9)
d(M–C21B)	1.995(9)	2.02(1)
d(M–N1A)	2.197(6)	2.169(7)
d(M–N2A)	1.975(6)	1.995(6)
d(M–N1B)	2.199(7)	2.159(8)
d(M–N2B)	1.980(6)	1.994(7)
∠(N2A–M–C21A)	78.2(3)	77.1(3)
∠(N2B–M–C21B)	78.6(3)	77.0(3)
∠(N1A–M–N2A)	77.9(3)	78.2(3)
∠(N1B–M–N2B)	77.5(3)	78.1(3)
∠(N2A–M–N2B)	168.8(3)	176.4(3)
∠(N1A–M–C21A)	156.0(3)	155.3(3)
∠(N1B–M–C21B)	155.5(3)	155.1(3)

Photophysical and electrochemical properties

Firstly, the photophysical behavior of complexes **[Ru]** and **[Os]** was investigated in dilute CH_3CN solution. The experimental electronic absorption and photoluminescence profiles are shown in Figure 3, while Table 2 summarizes the data collected for the two complexes as well as the proligand **HL**.

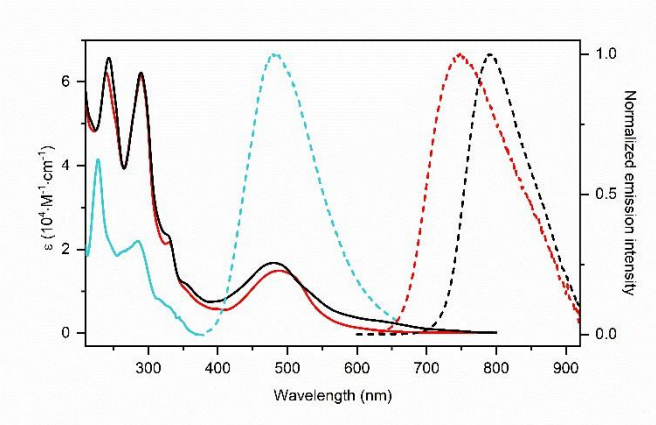

Figure 3. Electronic absorption (solid traces) and emission (dashed traces) spectra of complexes **[Ru]** (red) and **[Os]** (black) recorded for samples in dilute (2×10^{-5} M) degassed CH_3CN at room temperature upon excitation at λ_{exc} = 460 nm, presented alongside the proligand **HL** (cyan) in dilute (3×10^{-6} M) air-equilibrated CH_3CN at room temperature upon excitation at λ_{exc} = 340 nm.

In their absorption spectra, the two complexes are characterized by intense bands falling in the deep-UV region with absorption maxima in the range $\lambda_{abs,max}$ = 240–290 nm, ε = 6.6–6.2 and 5.0–6.2×10^4 M^{-1} cm^{-1} for **[Ru]** and **[Os]**, respectively. A broader, less intense band is present at much lower energies in the visible region with $\lambda_{abs,max}$ = 488 and 480 nm and ε of 1.5×10^4 and 1.7×10^4 M^{-1} cm^{-1} for **[Ru]** and **[Os]**, respectively. In comparison to **[Ru]**, complex **[Os]** displays an absorption tail that extends further in the visible spectrum and presents three progressively less intense shoulders at λ_{abs} *ca.* 530, 640, and 736 nm, with ε values not higher than 1.0×10^4 M^{-1} cm^{-1} and decreasing down to 6.4×10^3 M^{-1} cm^{-1} for the broadest shoulder in the longer wavelength flank. Effectively, this panchromatic absorption profile renders solutions of complex **[Os]** virtually black, while solutions of **[Ru]** appear brown in color.

The nature of these bands can be attributed by comparing these data with the electronic absorption spectra of the proligand **HL** (Figure 3). Firstly, the spectrum of both complexes and proligand **HL** displays structured absorption bands in the UV with almost identical energy (λ_{max} = 230, 285 nm), with about half of the intensity for the latter compared to the former due the fact that in the complexes two coordinated **L** ligands are present. This observation is a strong hint towards their singlet ligand-centered (^{1}LC) nature with $^1\pi\rightarrow\pi$ character being unaffected by coordination to Ru(II) and Os(II). Moving towards lower energies, the weaker and broader band seen in the complexes at λ_{abs} = 488–480 nm are instead absent in the proligand, and they can be attributed with confidence to singlet metal-to-ligand charge transfer transitions (^{1}MLCT) with $^1d_\pi\rightarrow\pi_{PhenPyd}^*$ character, where Phen and Pyd are the phenanthroline and pyridylidene moiety, respectively.[74] This band appears to be hypsochromically shifted by 340 cm^{-1} upon going from Ru(II) to Os(II), which may seem counterintuitive due to the lower oxidation potential of the latter (*vide infra*). Lastly, the very broad shoulders observed for complex **[Os]** are interpreted in terms of direct population of ^{3}MLCT states from spin-forbidden ($S_0\rightarrow T_1$) transitions.[75] This behavior is frequently reported for Os(II) polypyridine complexes as a result of the high SOC induced by the heavy metal, especially when compared with that of Ru(II).[19,37]

This analysis is further supported by time-dependent density functional theory (TD-DFT) calculations (see Supporting Information for further details). The computed transitions are listed in Tables S4–S6, and the nature of the electronic transitions according to THEODore analysis is shown in Figure S15–S16. Comparison between experimental and computed spectra are displayed in Figure 4. Moreover, frontier orbitals and the associated electron density difference maps (EDDMs) related to the main $S_0\rightarrow S_n$ transitions at the Franck-Condon geometry for complex **[Ru]** are depicted in Figure S17 and Figure S18, respectively. The three highest occupied MOs, namely HOMO-2, HOMO-1 and HOMO, are very close in energy and comprised within 0.1 eV. They are almost pure d orbitals of the ruthenium with little contribution arising from the ligand. On the contrary, occupied orbitals down to HOMO-5 lie much deeper in energy with a difference of more than 1 eV between the HOMO-2 and the HOMO-3, and exhibit an almost pure ligand character. The nature of the LUMOs is more homogeneous with mainly ligand character up to LUMO+5, though a very small contribution of the cation exists up to LUMO+3. The computed absorption spectrum of **[Ru]** presents multiple electronic transitions at low energy, such as $S_0\rightarrow S_1$ (λ = 542 nm, $^1d_\pi\rightarrow\pi_{Pyd}^*$) at and the most intense $S_0\rightarrow S_5$ (λ = 478 nm, $^1d_\pi\rightarrow\pi_{PhenPyd}^*$) and $S_0\rightarrow S_9$ (λ = 447 nm, $^1d_\pi\rightarrow\pi_{Phen}^*$), that convolute into the broad, weak bands observable at 400–500 nm with an extended tail up to 550 nm. Similarly, the band observed at around 350 nm is due to $S_0\rightarrow S_{17}$ (λ = 355 nm, $^1d_\pi\rightarrow\pi_{Phen}^*$) and $S_0\rightarrow S_{18}$ (λ = 346 nm, $^1d_\pi\rightarrow\pi_{Phen}^*$) transitions. Thus, all the computed states up to $S_0\rightarrow S_{18}$ are mainly of ^{1}MLCT character originating from HOMO-2 to HOMO towards LUMO to LUMO+5. Moving at higher energies, the transitions responsible for the band experimentally observed around λ = 320 nm are of admixed ^{1}LC and ^{1}LLCT character, and correspond to the computed excitations $S_0\rightarrow S_{19}$, $S_0\rightarrow S_{20}$, $S_0\rightarrow S_{21}$ and $S_0\rightarrow S_{22}$ at 327, 320, 318 and 310 nm, respectively and are generated by excitation coming from HOMO-5 to HOMO-3 towards the various LUMOs. The most intense bands computed are around 290 nm and correspond to the ^{1}LC transitions $S_0\rightarrow S_{34}$ (λ = 287 nm) and $S_0\rightarrow S_{35}$ (λ = 285 nm), the latter having a partial ^{1}MLCT character. These computations are negligibly affected by the inclusion of SOC perturbation. Overall, these attributions are in good agreement with the experimental findings.

A very similar picture can be drawn for the frontier orbitals and the electronic transitions computed for complex **[Os]** regarding the type and nature of the main absorption bands when no SOC perturbation is included, with intense ^{1}MLCT transitions associated to $S_0\rightarrow S_5$, $S_0\rightarrow S_7$ and, to a larger extent, $S_0\rightarrow S_9$, which are responsible for the absorption processes calculated at λ = 489, 469 and 465 nm, respectively (Table S4). The resulting absorption spectrum is bathochromically shifted compared to that of **[Ru]** in disagreement with what is observed experimentally (Figure 4). Nevertheless, introduction of SOC perturbation modifies the spectrum to a much larger extent for the Os derivative when compared to the Ru counterpart. Indeed, complex **[Os]** shows a higher degree of singlet-triplet mixing and the resulting spectrum displays a hypsochromic shift of the band at λ_{abs} around 450 nm due to the mixing of

the absorbing singlet states with higher lying triplet manifolds resulting in a spectrum that agrees well with the experimental finding. For both samples, the absorbance tail beyond λ_{abs} = 550 nm is assigned to transitions $S_0 \rightarrow T_n$. Larger SOC effect allows direct population of the triplet states for the **[Os]** derivative and provides a slightly more intense absorption tail that extends over the entire visible spectrum (Table S6).

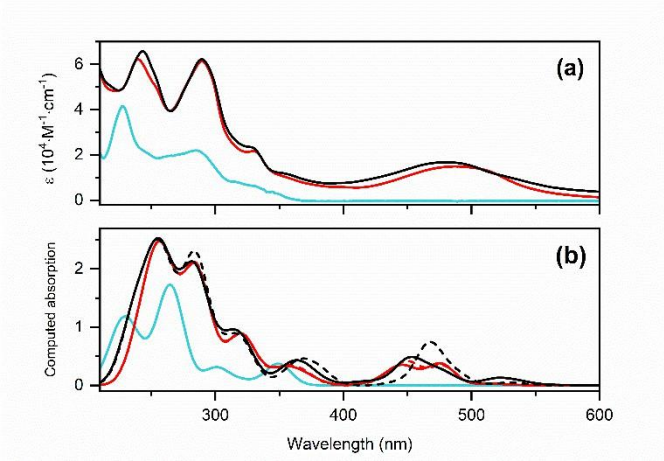

Figure 4. Comparison between the experimental UV-vis absorption spectra recorded for dilute CH_3CN samples (a) and computed spectra (b) of the proligand **HL** (cyan), complex **[Ru]** (red), and complex **[Os]** (black). Simulated spectra computed with and without SOC perturbation are displayed as dashed and solid traces, respectively.

The electrochemical properties of the complexes were investigated by means of cyclic voltammetry (CV) and the corresponding data are listed in Table 2. In the positive bias, both compounds show a reversible oxidation event at *E* = +1.09 and +0.87 V *vs.* SCE for **[Ru]** and **[Os]**, respectively, associated to the metal centered M^{II}/M^{III} process.[76] These values are cathodically shifted from related $[M(tpy)_2]^{2+}$ complexes (+1.30 and +0.97 V *vs.* SCE for M = Ru and Os, respectively)[77] which can be ascribed to the increased electron density on the metal exerted by the strongly donor pyridylidene units. As expected, the oxidation potential of **[Os]** appears less positive than that of **[Ru]** ($|\Delta E_{ox}|$ = *ca.* 0.2 V) since 5d orbitals are higher in energy that 4d orbitals.[37,78] In the negative bias, the observed irreversible waves match those of the precursor **HL** (see Figure S14 of the Supporting Information) and are formally ascribed to reduction events centered on the phenanthroline moiety.[79] A similar variation is observed for the reduction potentials of both complexes, with that of **[Os]** being anodically shifted by *ca.* 0.2 V, which could be indicative of a more intense d→π* ground-state interaction. The resulting electrochemical gap is ΔE = 2.09 eV (593 nm) and 2.05 eV (605 nm) for **[Ru]** and **[Os]**, respectively. These values correspond to the onset of the lowest-energy band, in agreement with the MLCT character assigned previously.

Both complexes are photostable and emissive in dilute air-equilibrated and degassed CH_3CN solution displaying a broad spectral profile, albeit with moderate PLQY. Complex **[Os]** shows an interesting emission in the NIR region with a broad featureless band at $\lambda_{em,\,max}$ = 790 nm and PLQY values of 0.6% in degassed solution, respectively. The experimental emission of complex **[Ru]** in solution is more hypsochromically shifted due to the larger stabilization of the metal-centered HOMO, but it still falls in the deep-red portion of the visible spectrum tailing into the NIR with a $\lambda_{em,\,max}$ = 747 nm and PLQY values of 0.2% for degassed samples, respectively.

The radiative process responsible for the above-described photoluminescence is ascribed to the lowest-lying ^{3}MLCT state, computed without SOC at λ_{em} = 780 and 789 nm for complex **[Ru]** and **[Os]**, respectively. The associated EDDMs and Theodore analysis are shown in Figure 5 and Figures S15–17 of the Supporting Information, respectively. As already observed for the lower-energy transitions at the Franck-Condon geometry, the T_1 state stems from an excitation from the metal (either Ru or Os) towards the ligand-based LUMO, which is mainly localized on one of the two ligands. Similar to what is observed for the absorption process, SOC perturbation negligibly influences the energy of the triplet state for the Ru(II) derivative, yet it yields to the splitting of the T_1 state into three substates components which all feature a computed emission wavelength of $\lambda_{em,theo,SOC}$ = 783 nm. A sharply different effect is observed instead for the Os(II) counterpart upon introduction of SOC effect, which gives rise to a large bathochromic shift of the emission wavelength with a sizeable energetic split of the three components computed at $\lambda_{em,theo,SOC}$ = 821, 817 and 814 nm (Table S7). These results allow us to clearly assign the bathochromic shift observed experimentally for the emission of **[Os]** compared to that of **C1** to the much larger SOC effects exerted by the Os(II) ion in the former complex.

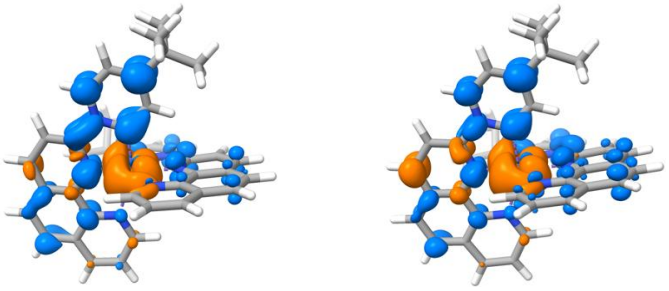

[Ru]
$T_1 \rightarrow S_0$

[Os]
$T_1 \rightarrow S_0$

Figure 5. EDDMs between the electronic T_1 and S_0 states both at T_1 geometry computed for complexes **[Ru]** (*left*) and **[Os]** (*right*). Electronically depleted and enriched areas are colored in blue and in orange, respectively.

Excited state decay kinetics could be fitted by means of a mono-exponential model providing lifetimes of τ = 129 and 62 ns for complex **[Ru]** and **[Os],** respectively, that shorten in the presence of quenching dioxygen molecules. Overall, these data allowed us to estimate the radiative (k_r) and non-radiative (k_{nr}) rate constants characterizing the emissive excited state, which have been calculated by using the following equations (1–2):

$$k_r = \frac{PLQY}{\tau} \quad \text{(eqn. 1)}$$

$$k_{nr} = \frac{1-PLQY}{\tau} \quad \text{(eqn. 2)}$$

It should be noted that while the k_r value for complex **[Ru]** was estimated experimentally to be 2×10^4 s^{-1}, for complex **[Os]** it is five times as much, with a value of 1.0×10^5 s^{-1}, highlighting the stronger SOC effect exerted by the heavier Os(II) center in agreement with the above-mentioned discussion. Furthermore, as listed in Table S7 of the Supporting Information, computed Boltzmann-averaged k_r values are in excellent agreement with the experimental ones.

Table 2. Photophysical and cyclovoltammetry data recorded for complexes **[Ru]**, **[Os]**, and proligand **HL** in dilute air-equilibrated (air) and degassed (deg) CH_3CN at room temperature. *sh* denotes a shoulder, *br* denotes a broad signal. The PLQY values have been calculated with $Ru(bpy)_3Cl_2$ as standard with a λ_{exc} = 480 nm.

	λ_{abs} (nm) (ε 10^3·M^{-1}·cm^{-1}) [a]	λ_{em} [nm]		PLQY (%)		τ_{obs} [ns]	τ_{obs} [ns]	k_r [10^5 s^{-1}]	k_{nr} [10^6 s^{-1}]	E_{ox} (M^{III}/M^{II}) [V][b]	E_{red} [V]	ΔE [eV][c]
		air	*deg*	*air*	*deg*	*air*	*deg*	*deg*	*deg*			
[Ru]	239 (62.2), 253*sh* (50.6), 289 (61.4), 330 (21.7), 354*sh* (10.4), 488 (14.9)	747	747	0.1	0.22	84	129	0.2	7.7	+ 1.03 (rev, ΔEp = 72 mV)	-1.00 (irrev) -1.55 (irrev)	2.09
[Os]	243 (65.8), 289 (62.2), 329*sh* (23.3), 356*sh* (11.6), 480 (16.8), 528*sh* (10.3), 640*sh* (2.67), 736*sh* (0.64)	790	790	0.5	0.6	49	62	1.0	16.0	+ 0.87 (rev, ΔEp = 65 mV)	-1.18 (irrev) -1.56 (irrev)	2.05
HL	228 (41.5), 285 (21.9), 315*sh* (8.13), 331*sh* (6.21)	482								–	-1.00 (irrev) -1.68 (irrev)	

[a] *sh* denotes a shoulder. [b]Potentials are quoted *vs* SCE. Under these conditions, $E_{1/2\ (Fc+/Fc)}$ = 0.39 V. Recorded in CH_3CN using NBu_4PF_6 0.1 M as supporting electrolyte at 100 mV s^{-1}. [c] Electrochemical band gap ($\Delta E = E_{ox} - E_{red1}$).

Both complexes are stable and emissive upon irradiation in the solid state and in frozen glassy matrix in MeTHF at 77 K. Table 3 summarizes the corresponding photophysical data. Selected emission spectra for the complexes are presented in Figure 6, while the spectra relative to the proligand **HL** are shown in Figure S13 of the Supporting Information. Upon lowering the temperature down to 77 K, both complexes display a clear hypsochromic shift of their emission with maximum at λ_{em} = 715 and 754 nm, and concomitant prolongation of the lifetime being its average value, $\bar{\tau}$, as long as 2.69 μs and 337 ns, for complex **[Ru]** and **[Os]**, respectively. The structure of the emission profile of **[Ru]**, although with little resolution, can be attributed to the vibronic progression involving ligand modes. Overall, these data allowed us to ascribe the radiative process to arising from an emissive excited state with large ^{3}MLCT character. Furthermore, the increase in the excited state lifetimes at 77 K suggests the existence of closer-lying quenching states at room temperature for both complexes.[21,37] However, the remarkably higher lifetime increase for **[Ru]** reveals that these deactivation channels must remain more thermally-accessible at room-temperature in this complex due to the closer energetic proximity with the emissive ^{3}MLCT manifold, which would justify its lower PLQY respect to **[Os]**.

On the other hand, a sharply distinct behaviour between the two complexes was identified in the solid-state as crystalline samples (Figure 6). While the emission profile of complex **[Ru]** is virtually identical to that in CH_3CN solution, the one of complex **[Os]** is shifted squarely in the NIR region achieving an emission wavelength maximum as long as λ_{em} = 840 nm. The different crystal structures may account for these sizeably different spectra. In fact, one can hypothesize that the closer interaction between the Phen moiety of the ligand and the PF_6^- anion in complex **[Ru]** compared to **[Os]** is expected to destabilize the ^{3}MLCT state, thus resulting in a noticeable hypsochromic shift of the emission for **[Ru]** (*cf.* Figure S11 and S12 of the Supporting Information). Due to their weak nature and the technical limitation that are faced in detecting NIR emission, the PLQY values of these solid-state samples could not be determined with our setup regrettably.

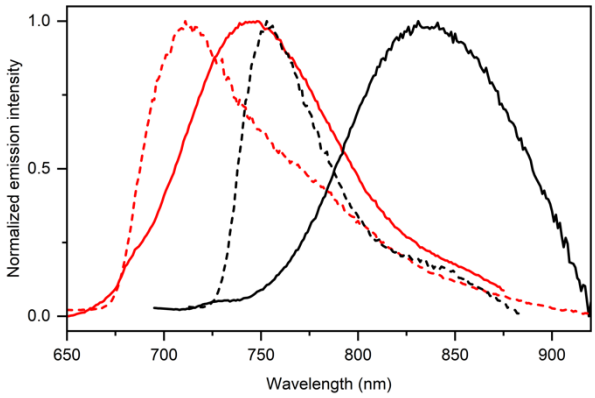

Figure 6. Emission spectra of complexes **[Ru]** (red traces) and **[Os]** (black traces) in MeTHF glassy matrix at 77 K (dashed traces) upon excitation at λ_{exc} = 480 nm, and in the solid state as crystalline samples (solid traces) upon excitation at λ_{exc} = 540 and 500 nm, respectively.

Table 3. Photophysical data recorded for complexes **[Ru]**, **[Os]**, and proligand **HL** as neat powders and in MeTHF glassy matrix at 77K.

	λ_{em} [nm]		τ_{obs} (%A_{rel})		$\bar{\tau}$	
	crystalline powder	77 K (MeTHF)	crystalline powder	77 K (MeTHF)	crystalline powder	77 K (MeTHF)
[Ru]	745	715	299 μs (10%) 50.0 μs (30%) 8.7 μs (59%)	4.75 μs (12%) 2.0 μs (49%) 0.6 μs (39%)	196 μs	2.69 μs
[Os]	840	754	34.2 μs (13%) 4.5 μs (87%)	446 ns (31%) 184 ns (40%) 44.1 ns (29%)	20.1 μs	337 ns
HL	445	406	8.1 ns (47%) 4.5 ns (53%)	11.6 ns (6%) 4.0 ns (46%) 1.3 ns (47%)	6.7 ns	5.3 ns

Conclusion

In summary, a novel design strategy is proposed for achieving NIR photoluminescence with transition metal complexes, based on the unprecedented use of the unconventional NHC-based pyridylidene moiety in combination with the low-lying π-accepting phenanthroline scaffold. Coordination of the engineered tridentate C^N^N ligand onto the metal ion occurs straightforwardly with concomitant C–H activation at the NHC site, yielding to charge neutral homoleptic Ru(II) and Os(II) complexes that crystallize as a racemate. Both target complexes displayed long-lived NIR luminescence arising from an excited state with ^{3}MLCT character. Interestingly, both absorption and emission profile are shifted to longer wavelengths for the Os(II) derivative when compared to the Ru(II) congener due to the larger SOC effect exerted by the heavier metal as also supported by TD-DFT calculation including SOC perturbation. As a consequence, emission spectrum of the Os(II) complex squarely fell in the NIR region with a maximum that reached 840 nm in crystalline samples, remarkably. This finding represents a rare example of Os(II) complexes that display PL spectra with emission wavelength maximum beyond 800 nm. Overall, the proposed ligand and complex design strategy appeared to be promising for the preparation of NIR emissive molecular species in both solution and solid state with appealing potential applications. Therefore, ongoing efforts in our research group are dedicated to improve the luminescence efficiency by rigidifying the coordinating sphere or improving the metal-ligand interaction.

Experimental section

Solvents were purified by standard procedures and purged with argon before use. All other chemicals used in this work were of analytical grade and were used without further purification until or unless stated, and all complexation reactions were performed under an inert atmosphere of argon. Chromatographic separations were carried out on silica gel (60–120 mesh). ^{1}H (400 MHz) and ^{13}C NMR (100 MHz) spectra were taken on a DRX400 Bruker spectrometer at ambient temperature. High-resolution mass spectrometry (HRMS) data was obtained by using Bruker micrOTOF-Q spectrometer.

Absorption spectra were recorded using a Perkin Elmer Lambda 950 double-beam UV-VIS spectrophotometer and baseline corrected. Steady-state emission spectra were recorded on a Horiba Jobin−Yvon IBH FL-322 Fluorolog 3 spectrometer equipped with a 450 W xenon arc lamp, double-grating excitation, and emission monochromators (2.1 nm mm^{-1} of dispersion; 1200 grooves mm^{-1}) and a Hamamatsu R13456 red sensitive Peltier-cooled PMT detector. Emission and excitation spectra were corrected for source intensity (lamp and grating) and emission spectral response (detector and grating) by standard correction curves. Time-resolved measurements were performed using either the Time-Correlated Single-Photon Counting (TCSPC) or the Multi-Channel Scaling

(MCS) electronics option of the TimeHarp 260 board installed on a PicoQuant FluoTime 300 fluorimeter (PicoQuant GmbH, Germany), equipped with a PDL 820 laser pulse driver. A pulsed laser diode LDH-P-C-445 (λ = 445 nm, pulse full width at half maximum <50 ps, repetition rate 200 kHz–40 MHz) was used to excite the sample and mounted directly on the sample chamber at 90°. The photons were collected by a PMA Hybrid-07 single photon counting detector. The data were acquired by using the commercially available software EasyTau II (PicoQuant GmbH, Germany), while data analysis was performed using the built-in software FluoFit (PicoQuant GmbH, Germany). All the solvents were spectrophotometric grade. Dearated samples were prepared by the freeze–pump–thaw technique by using a home-made quartz cuvette equipped with a Rotaflo stopcock.

All calculations have been performed with ADF 2019at DFT level of theory (B3LYP functional) with inclusion of scalar relativistic effects with ZORA hamiltonian. All atoms were described by the TZP basis set. Weak interactions were included using Grimme's corrections. The solvent (CH_3CN) was introduced using the COSMO model. The quality of the DFT grid was set to good. All geometries were fully optimized and the absorption spectra computed by mean of TD-DFT on the encountered minima. The emission wavelength was computed by optimization of the lowest triplet state by the same methodology. Nature of the electronic transitions was determined by THEODore analysis and the electron difference density maps was computed using the Dgrid package.

Deposition Numbers (https://www.ccdc.cam.ac.uk/services/structures?id=doi:10.1002/chem.202501791R1) 2431775 (for **[Ru]**) and 2431780 (for **[Os]**), contain the supplementary crystallographic data for this paper. These data are provided free of charge by the joint Cambridge Crystallographic Data Centre and Fachinformationszentrum Karlsruhe (http://www.ccdc.cam.ac.uk/structures) Access Structures service.

Supporting Information

The authors have cited additional references within the Supporting Information.[80–89]

Acknowledgements

C.C. and P.C.G. are grateful to the French Agence Nationale de la Recherche (ANR) for funding the project ANR 21-CE50-0040 "SunHy" that covers S.S.J. contract. M.M. gratefully acknowledges the Université de Strasbourg and CNRS for financial support, and the French Agence Nationale de la Recherche (ANR) for funding the grants ANR-20-CE29-0021 "PhotoMecha", ANR-21-CE29-0015 "ChirON" and ANR-24-CE29-2108 "E-Polar". The College Doctoral of the Université de Strasbourg is kindly acknowledged for co-funding the PhD contract of V.G. C.G. thanks the HPC of Strasbourg for computational time. The authors are also grateful to S. Parant for the electrochemical experiments, F. Dupire (mass spectrometry MassLor platform, Lorraine University), and A. Doudouh and E. Wenger (PMD^2X X-ray diffraction facility of pôle CPM, University of Lorraine) for X-ray diffraction measurements, data processing and analysis, and providing reports for publication: http://crm2.univ-lorraine.fr/lab/fr/ services/pmd2x).

Keywords: carbene complexes • near infrared emitters • photophysics • ruthenium complexes • osmium complexes

[1] C. A. Bignozzi, R. Argazzi, R. Boaretto, E. Busatto, S. Carli, F. Ronconi, S. Caramori, *Coord. Chem. Rev.* 2013, *257*, 1472–1492.
[2] C. E. Housecroft, E. C. Constable, *Chem. Sci.* 2022, *13*, 1225–1262.
[3] K. E. Dalle, J. Warnan, J. J. Leung, B. Reuillard, I. S. Karmel, E. Reisner, *Chem. Rev.* 2019, *119*, 2752–2875.
[4] C. K. Prier, D. A. Rankic, D. W. C. MacMillan, *Chem. Rev.* 2013, *113*, 5322–5363.
[5] K. Rybicka-Jasińska, W. Shan, K. Zawada, K. M. Kadish, D. Gryko, *J. Am. Chem. Soc.* 2016, *138*, 15451–15458.
[6] D. Kim, V. Q. Dang, T. S. Teets, *Chem. Sci.* 2024, *15*, 77–94.
[7] D. L. Ashford, M. K. Gish, A. K. Vannucci, M. K. Brennaman, J. L. Templeton, J. M. Papanikolas, T. J. Meyer, *Chem. Rev.* 2015, *115*, 13006–13049.
[8] M. Mauro, A. Aliprandi, D. Septiadi, N. S. Kehr, L. De Cola, *Chem Soc Rev* 2014, *43*, 4144–4166.
[9] N. A. Yusoh, M. R. Gill, X. Tian, *Chem. Soc. Rev.* 2025, *54*, 3616–3646.
[10] H. Yersin, Ed. , *Highly Efficient OLEDs with Phosphorescent Materials*, Wiley, 2007.
[11] C. Bizzarri, E. Spuling, D. M. Knoll, D. Volz, S. Bräse, *Coord. Chem. Rev.* 2018, *373*, 49–82.
[12] X. Li, Y. Xie, Z. Li, *Chem. – Asian J.* 2021, *16*, 2817–2829.
[13] H. Xiang, J. Cheng, X. Ma, X. Zhou, J. J. Chruma, *Chem. Soc. Rev.* 2013, *42*, 6128.
[14] A. Barbieri, E. Bandini, F. Monti, V. K. Praveen, N. Armaroli, *Top. Curr. Chem.* 2016, *374*, 47.
[15] M. Ibrahim-Ouali, F. Dumur, *Molecules* 2019, *24*, 1412.
[16] M. Fagnoni, *Angew. Chem. Int. Ed.* 2010, *49*, 6709–6710.

[17] R. Englman, J. Jortner, *Mol. Phys.* 1970, *18*, 145–164.
[18] S. Campagna, F. Puntoriero, F. Nastasi, G. Bergamini, V. Balzani, in *Photochem. Photophysics Coord. Compd. I* (Eds.: V. Balzani, S. Campagna), Springer Berlin Heidelberg, Berlin, Heidelberg, 2007, pp. 117–214.
[19] D. Kumaresan, K. Shankar, S. Vaidya, R. H. Schmehl, in *Photochem. Photophysics Coord. Compd. II* (Eds.: V. Balzani, S. Campagna), Springer Berlin Heidelberg, Berlin, Heidelberg, 2007, pp. 101–142.
[20] Y. Chi, P.-T. Chou, *Chem. Soc. Rev.* 2007, *36*, 1421.
[21] D. W. Thompson, A. Ito, T. J. Meyer, *Pure Appl. Chem.* 2013, *85*, 1257–1305.
[22] M. Maestri, N. Armaroli, V. Balzani, E. C. Constable, A. M. W. C. Thompson, *Inorg. Chem.* 1995, *34*, 2759–2767.
[23] J.-P. Collin, R. Kayhanian, J.-P. Sauvage, G. Calogero, F. Barigelletti, A. D. Cian, J. Fischer, *Chem. Commun.* 1997, 775–776.
[24] S. H. Wadman, M. Lutz, D. M. Tooke, A. L. Spek, F. Hartl, R. W. A. Havenith, G. P. M. Van Klink, G. Van Koten, *Inorg. Chem.* 2009, *48*, 1887–1900.
[25] D. G. Brown, N. Sanguantrakun, B. Schulze, U. S. Schubert, C. P. Berlinguette, *J. Am. Chem. Soc.* 2012, *134*, 12354–12357.
[26] L. Hammarström, O. Johansson, *Coord. Chem. Rev.* 2010, *254*, 2546–2559.
[27] T. Schlotthauer, B. Suchland, H. Görls, G. A. Parada, L. Hammarström, U. S. Schubert, M. Jäger, *Inorg. Chem.* 2016, *55*, 5405–5416.
[28] M. Majuran, G. Armendariz- Vidales, S. Carrara, M. A. Haghighatbin, L. Spiccia, P. J. Barnard, G. B. Deacon, C. F. Hogan, K. L. Tuck, *ChemPlusChem* 2020, *85*, 346–352.
[29] T. J. Meyer, *Pure Appl. Chem.* 1986, *58*, 1193–1206.
[30] J. N. Demas, B. A. DeGraff, *Anal. Chem.* 1991, *63*, 829A-837A.
[31] S. M. Draper, D. J. Gregg, E. R. Schofield, W. R. Browne, M. Duati, J. G. Vos, P. Passaniti, *J. Am. Chem. Soc.* 2004, *126*, 8694–8701.
[32] S. D. Bergman, D. Gut, M. Kol, C. Sabatini, A. Barbieri, F. Barigelletti, *Inorg. Chem.* 2005, *44*, 7943–7950.
[33] A. Mamo, A. Juris, G. Calogero, S. Campagna, *Chem. Commun.* 1996, 1225.
[34] M. I. J. Polson, E. A. Medlycott, G. S. Hanan, L. Mikelsons, N. J. Taylor, M. Watanabe, Y. Tanaka, F. Loiseau, R. Passalacqua, S. Campagna, *Chem. – Eur. J.* 2004, *10*, 3640–3648.
[35] A. K. Pal, S. Serroni, N. Zaccheroni, S. Campagna, G. S. Hanan, *Chem Sci* 2014, *5*, 4800–4811.
[36] Y. Yuan, J. Liao, S. Ni, A. K. - Y. Jen, C. Lee, Y. Chi, *Adv. Funct. Mater.* 2020, *30*, 1906738.
[37] F. Glaser, S. De Kreijger, K. Achilleos, L. N. Satheesh, A. Ripak, N. Chantry, C. Bourgois, S. Quiquempoix, J. Scriven, J. Rubens, M. Vander Wee- Léonard, M. Daenen, M. Gillard, B. Elias, L. Troian- Gautier, *ChemPhotoChem* 2024, *8*, e202400134.
[38] P. A. Scattergood, J. Roberts, S. A. E. Omar, P. I. P. Elliott, *Inorg. Chem.* 2019, *58*, 8607–8621.
[39] C. Kreitner, E. Erdmann, W. W. Seidel, K. Heinze, *Inorg. Chem.* 2015, *54*, 11088–11104.
[40] R. M. O'Donnell, P. G. Johansson, M. Abrahamsson, G. J. Meyer, *Inorg. Chem.* 2013, *52*, 6839–6848.
[41] A. Damas, M. P. Gullo, M. N. Rager, A. Jutand, A. Barbieri, H. Amouri, *Chem. Commun.* 2013, *49*, 3796.
[42] F. Barigelletti, B. Ventura, J.-P. Collin, R. Kayhanian, P. Gaviña, J.-P. Sauvage, *Eur. J. Inorg. Chem.* 2000, *2000*, 113–119.
[43] J.-L. Chen, Y. Chi, K. Chen, Y.-M. Cheng, M.-W. Chung, Y.-C. Yu, G.-H. Lee, P.-T. Chou, C.-F. Shu, *Inorg. Chem.* 2010, *49*, 823–832.
[44] J.-L. Liao, Y. Chi, C.-C. Yeh, H.-C. Kao, C.-H. Chang, M. A. Fox, P. J. Low, G.-H. Lee, *J. Mater. Chem. C* 2015, *3*, 4910–4920.
[45] P. Chou, Y. Chi, *Chem. – Eur. J.* 2007, *13*, 380–395.
[46] K. C. D. Robson, B. D. Koivisto, A. Yella, B. Sporinova, M. K. Nazeeruddin, T. Baumgartner, M. Grätzel, C. P. Berlinguette, *Inorg. Chem.* 2011, *50*, 5494–5508.

[47] T. Schlotthauer, G. A. Parada, H. Görls, S. Ott, M. Jäger, U. S. Schubert, *Inorg. Chem.* 2017, *56*, 7720–7730.
[48] T. Lee, J. Hung, Y. Chi, Y. Cheng, G. Lee, P. Chou, C. Chen, C. Chang, C. Wu, *Adv. Funct. Mater.* 2009, *19*, 2639–2647.
[49] S. A. E. Omar, P. A. Scattergood, L. K. McKenzie, C. Jones, N. J. Patmore, A. J. H. M. Meijer, J. A. Weinstein, C. R. Rice, H. E. Bryant, P. I. P. Elliott, *Inorg. Chem.* 2018, *57*, 13201–13212.
[50] A. Collado, A. Gómez-Suárez, A. R. Martin, A. M. Z. Slawin, S. P. Nolan, *Chem. Commun.* 2013, *49*, 5541.
[51] H. Amouri, *Chem. Rev.* 2023, *123*, 230–270.
[52] H. V. Huynh, *Chem. Rev.* 2018, *118*, 9457–9492.
[53] M. Elie, J.-L. Renaud, S. Gaillard, *Polyhedron* 2018, *140*, 158–168.
[54] S. U. Son, K. H. Park, Y.-S. Lee, B. Y. Kim, C. H. Choi, M. S. Lah, Y. H. Jang, D.-J. Jang, Y. K. Chung, *Inorg. Chem.* 2004, *43*, 6896–6898.
[55] V. Friese, S. Nag, J. Wang, M. Santoni, A. Rodrigue- Witchel, G. S. Hanan, F. Schaper, *Eur. J. Inorg. Chem.* 2011, *2011*, 39–44.
[56] G. J. Barbante, P. S. Francis, C. F. Hogan, P. R. Kheradmand, D. J. D. Wilson, P. J. Barnard, *Inorg. Chem.* 2013, *52*, 7448–7459.
[57] R. G. Alabau, B. Eguillor, J. Esler, M. A. Esteruelas, M. Oliván, E. Oñate, J.-Y. Tsai, C. Xia, *Organometallics* 2014, *33*, 5582–5596.
[58] L.-H. Chung, S.-C. Chan, W.-C. Lee, C.-Y. Wong, *Inorg. Chem.* 2012, *51*, 8693–8703.
[59] L.-H. Chung, K.-S. Cho, J. England, S.-C. Chan, K. Wieghardt, C.-Y. Wong, *Inorg. Chem.* 2013, *52*, 9885–9896.
[60] Á. Vivancos, C. Segarra, M. Albrecht, *Chem. Rev.* 2018, *118*, 9493–9586.
[61] J. A. Cabeza, I. del Río, E. Pérez- Carreño, M. G. Sánchez- Vega, D. Vázquez- García, *Angew. Chem. Int. Ed.* 2009, *48*, 555–558.
[62] C.-H. Tseng, M. A. Fox, J.-L. Liao, C.-H. Ku, Z.-T. Sie, C.-H. Chang, J.-Y. Wang, Z.-N. Chen, G.-H. Lee, Y. Chi, *J. Mater. Chem. C* 2017, *5*, 1420–1435.
[63] A. J. Arduengo, R. L. Harlow, M. Kline, *J. Am. Chem. Soc.* 1991, *113*, 361–363.
[64] J. Lorkowski, L. Gojiashvili, P. Yorkgitis, D. Pichon, J. Talcik, M. Gembicky, T. Roisnel, O. Baslé, R. Jazzar, M. Mauduit, G. Bertrand, *J. Am. Chem. Soc.* 2025, *147*, 14972–14977.
[65] T. Koizumi, T. Tomon, K. Tanaka, *Organometallics* 2003, *22*, 970–975.
[66] D. Tapu, D. A. Dixon, C. Roe, *Chem. Rev.* 2009, *109*, 3385–3407.
[67] J. V. Ros- Lis, R. Martínez- Máñez, J. Soto, C. McDonagh, A. Guckian, *Eur. J. Inorg. Chem.* 2006, *2006*, 2647–2655.
[68] T. J. Mooibroek, C. A. Black, P. Gamez, J. Reedijk, *Cryst. Growth Des.* 2008, *8*, 1082–1093.
[69] J. Montagu, G. Gontard, J. A. G. Williams, J. Moussa, *Eur. J. Inorg. Chem.* 2023, *26*, e202300487.
[70] D. A. Bardwell, A. M. W. C. Thompson, J. C. Jeffery, J. A. McCleverty, M. D. Ward, *J Chem Soc Dalton Trans* 1996, 873–878.
[71] A. McSkimming, G. E. Ball, M. M. Bhadbhade, S. B. Colbran, *Inorg. Chem.* 2012, *51*, 2191–2203.
[72] K. Lashgari, M. Kritikos, R. Norrestam, T. Norrby, *Acta Crystallogr. C* 1999, *55*, 64–67.
[73] N. G. S. Mateyise, M. M. Conradie, J. Conradie, *Molecules* 2024, *29*, 5078.
[74] M. Montalti, A. Credi, L. Prodi, M. T. Gandolfi, *Handbook of Photochemistry*, CRC Press, 2006.
[75] A. B. Maurer, G. J. Meyer, *J. Am. Chem. Soc.* 2020, *142*, 6847–6851.
[76] A. Juris, V. Balzani, F. Barigelletti, S. Campagna, P. Belser, A. Von Zelewsky, *Coord. Chem. Rev.* 1988, *84*, 85–277.
[77] J. P. Sauvage, J. P. Collin, J. C. Chambron, S. Guillerez, C. Coudret, V. Balzani, F. Barigelletti, L. De Cola, L. Flamigni, *Chem. Rev.* 1994, *94*, 993–1019.
[78] S. Francis, C. R. Rice, P. A. Scattergood, P. I. P. Elliott, *Dalton Trans.* 2022, *51*, 13692–13702.
[79] K. G. Von Eschwege, J. Conradie, *Electrochem. Commun.* 2022, *136*, 107225.
[80] G. A. Crosby, J. N. Demas, *J. Am. Chem. Soc.* 1970, *92*, 7262–7270.
[81] H. Ishida, S. Tobita, Y. Hasegawa, R. Katoh, K. Nozaki, *Coord. Chem. Rev.* 2010, *254*, 2449–2458.
[82] J. R. Lakowicz, J.R., in Princ. Fluoresc. Spectrosc. 3rd Ed Springer N. Y. 2006.

[83] G. Te Velde, F. M. Bickelhaupt, E. J. Baerends, C. Fonseca Guerra, S. J. A. Van Gisbergen, J. G. Snijders, T. Ziegler, *J. Comput. Chem.* 2001, *22*, 931–967.
[84] P. J. Stephens, F. J. Devlin, C. F. Chabalowski, M. J. Frisch, *J. Phys. Chem.* 1994, *98*, 11623–11627.
[85] E. Van Lenthe, E. J. Baerends, *J. Comput. Chem.* 2003, *24*, 1142–1156.
[86] E. Van Lenthe, A. Ehlers, E.-J. Baerends, *J. Chem. Phys.* 1999, *110*, 8943–8953.
[87] S. Grimme, J. Antony, S. Ehrlich, H. Krieg, *J. Chem. Phys.* 2010, *132*, 154104.
[88] F. Plasser, *J. Chem. Phys.* 2020, *152*, 084108.
[89] M. Kohout, DGRID, version 4.6, MaxPlanck Society, Radebeul, Germany, 2011.

Entry for the Table of Contents

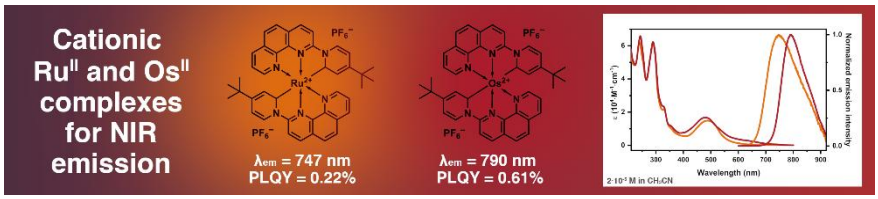

Readily accessed Ru(II) and Os(II) phenanthroline-pyridylidene complexes exhibited Near Infrared Luminescence up to 840 nm.